Xyloglucans and Microtubules Synergistically Maintain Meristem Geometry and Phyllotaxis[1][OPEN]

Feng Zhao,[a,2] Wenqian Chen,[a,2] Julien Sechet,[b] Marjolaine Martin,[a] Simone Bovio,[a] Claire Lionnet,[a] Yuchen Long,[a] Virginie Battu,[a] Grégory Mouille,[b] Françoise Monéger,[a] and Jan Traas[a,3,4]

[a]Laboratoire de Reproduction et Développement des Plantes, Université de Lyon, ENS de Lyon, UCBL, INRA, CNRS, 69364 Lyon cedex 07, France

[b]Institut Jean-Pierre Bourgin, UMR1318 INRA-AgroParisTech, ERL3559 CNRS Bâtiment 1, INRA Centre de Versailles-Grignon, 78026 Versailles cedex, France

ORCID IDs: 0000-0001-5180-2095 (F.Z.); 0000-0001-8398-4743 (J.S.); 0000-0002-9836-6742 (S.B.); 0000-0001-5071-4632 (Y.L.); 0000-0002-5493-754X (G.M.); 0000-0003-2107-5696 (F.M.); 0000-0001-5107-1472 (J.T.).

The shoot apical meristem (SAM) gives rise to all aerial plant organs. Cell walls are thought to play a central role in this process, translating molecular regulation into dynamic changes in growth rate and direction, although their precise role in morphogenesis during organ formation is poorly understood. Here, we investigated the role of xyloglucans (XyGs), a major, yet functionally poorly characterized, wall component in the SAM of Arabidopsis (*Arabidopsis thaliana*). Using immunolabeling, biochemical analysis, genetic approaches, microindentation, laser ablation, and live imaging, we showed that XyGs are important for meristem shape and phyllotaxis. No difference in the Young's modulus (i.e. an indicator of wall stiffness) of the cell walls was observed when XyGs were perturbed. Mutations in enzymes required for XyG synthesis also affect other cell wall components such as cellulose content and pectin methylation status. Interestingly, control of cortical microtubule dynamics by the severing enzyme KATANIN became vital when XyGs were perturbed or absent. This suggests that the cytoskeleton plays an active role in compensating for altered cell wall composition.

The shoot apical meristem (SAM) gives rise to all aerial organs of the plant. It harbors a pool of stem cells located at the meristem summit that continuously self-renew and contribute to the formation of new organs (Pfeiffer et al., 2017). These organs are initiated in highly ordered patterns through a process called phyllotaxis. Organ positioning is the result of complex interactions between several hormonal pathways (Galvan-Ampudia et al., 2016). In particular auxin is essential in this process. This hormone accumulates at specific positions through active transport, where it initiates new organs through the activation of a regulatory molecular network (Reinhardt et al., 2003; de Reuille et al., 2006; La Rota et al., 2011). How this molecular regulation is then translated into specific growth patterns is not well understood, but it is well established that the cell wall plays a central role (Braybrook and Peaucelle, 2013; Armezzani et al., 2018; Cosgrove, 2018).

The cell wall is composed of relatively stiff cellulose microfibrils, embedded in a visco-elastic matrix of polysaccharides (Cosgrove, 2018). In meristematic tissues, cellulose is the most abundant cell wall component, making up 30% of the wall polysaccharides (Yang et al., 2016). The matrix is largely composed of xyloglucans, pectins, and arabinans, which each make up about 15% of the cell wall (Yang et al., 2016). Work over the last decades has revealed the complexity of wall dynamics, and although significant progress has been made, many questions remain concerning the global coordination of wall composition as well as the role of the individual components. The role of cellulose has been relatively well established (Baskin, 2005; McFarlane et al., 2014). The fibrils can be deposited in different arrangements, from completely random to highly aligned arrays. Because of their stiffness, they restrict growth along their length and their orientation largely defines growth directions. Pectins form an important part of the matrix surrounding the cellulose fibrils (Rizk et al., 2000 ; Cumming et al., 2005). Their precise interaction with other wall components is still not completely understood, but there is

[1]This work was supported by 'Morphodynamics' European Research Council grant no. 294397 (to F.Z., W.C., and J.T.); European Research Council grant 'PhyMorph' to Arezki Boudaoud (to Y.L.); and a Marie-Curie FP7 COFUND and AgreenSkills+ fellowship (609398 to J.S.).

[2]These authors contributed equally to this article.

[3]Author for contact: Jan.Traas@ens-lyon.fr.

[4]Senior authors.

The author responsible for distribution of materials integral to the findings presented in this article in accordance with the policy described in the Instructions for Authors (www.plantphysiol.org) is: Jan Traas (jan.traas@ens-lyon.fr).

F.Z. and W.C. designed and performed experiments and participated in writing; J.S. and G.M. performed the cell wall analysis; S.B., C.L., and Y.L. participated in imaging experiments; M.M. and V.B. performed genetic analysis; F.M. and J.T. conceived the project and participated in writing the article.

[OPEN]Articles can be viewed without a subscription.

www.plantphysiol.org/cgi/doi/10.1104/pp.19.00608

strong evidence that pectins participate in regulating organogenesis at the SAM (Peaucelle et al., 2011; Braybrook and Peaucelle, 2013).

Here we focus on the other major matrix component, xyloglucans (XyGs). XyGs are composed of chains of Glc molecules attached through beta (1 to 4) links, with different sugars as side chains such as Xyl, Gal, or Fuc. They are thought to play a role in both tethering the cellulose microfibrils to other components and in keeping the fibrils separated (Cosgrove, 2018). Their synthesis is controlled by several enzymes. In particular, *Xyloglucan α-Xylosyltransferase 1* (*XXT1*) and *XXT2* encode enzymes with α-xylosyltransferase activity that are capable of forming nascent XyG oligosaccharides, and their activity is required for XyG synthesis (Faik et al., 2002). Another gene, *α-XYLOSIDASE 1* (*XYL1*), encodes an α-xylosidase that removes the Xyl side chains, which block the degradation of the backbone (Minic et al., 2004).

The precise function of XyGs remains controversial. There are several indications that they play important roles. For instance, genes encoding xyloglucan endotransglucosylases/hydrolases, involved in remodeling the XyGs, are abundantly expressed at the shoot apical meristem (Armezzani et al., 2018). Moreover, Xiao et al. (2016) revealed that loss of xyloglucan in the *xxt1xxt2* double mutant affects cell wall integrity, the stability of the microtubule cytoskeleton, and the production and patterning of cellulose in primary cell walls in hypocotyls. However, other observations seem to question the role of xyloglucan in morphogenetic events. These include genetic analyses involving mutants of key enzymes required for XyG homeostasis. The *xxt1xxt2* mutant has in the end only a relatively minor growth phenotype compared with what could be expected in the absence of XyGs (Cavalier et al., 2008; Park and Cosgrove, 2012). Likewise, the *xyl1* knock-out mutant showing important modifications in XyG composition (Sampedro et al., 2010 ; Sampedro et al., 2001; Sechet et al., 2016) is able to form fertile plants.

The SAM, characterized by complex shape changes and growth patterns, offers the possibility to assess wall dynamics and XyG function in a rich developmental context. Using immunolabeling, biochemical analysis, and genetic approaches, we show that xyloglucans are differentially distributed across the inflorescence meristem, whereas cellulose and pectins do not appear to exhibit specific distribution patterns. In addition, we have used the *xxt1xxt2* double mutant and the *xyl1* mutant, both perturbed in XyG synthesis as discussed above. The analysis reveals a role for XyG homeostasis in meristem geometry and phyllotaxis. It also points at an active role of the cytoskeleton in compensating for altered wall composition.

RESULTS

Xyloglucan Distribution Patterns Correlate with Functional Domains at the Shoot Apical Meristem

We first examined the distribution of different types of xyloglucans in the wild-type SAM using immunolabeling with three different antibodies (LM15, LM25, and LM24) recognizing different xyloglucan residues with different affinities (Fig. 1A; Pedersen et al., 2012). For this purpose, we used both tissue sections and whole mount tissues (representative images are shown in Fig. 1, C and D, respectively; see Supplemental Figs. S1–S3 for more examples).

In Col-0 specific patterns were observed:

- The XXXG epitope recognized by LM15 was present throughout the SAM, most strongly in the inner tissues and less in the epidermis and primordia (Fig. 1, B and C; Supplemental Figs. S1 and S2). Labeling was particularly striking in differentiating cells at the meristem base, which probably corresponds to the rib meristem. Whole mount labeling allowed us to focus on the signal in the epidermis, which was relatively weak compared with the labeling of internal cells. Based on the three dimensional (3D) projection of whole mount signals at the SAM surface, we also found that the XXXG epitope was more abundant in older walls compared with those that had formed more recently throughout the meristem (Fig. 1D; Supplemental Figs. S1 and S3). This might be in part caused by the differences in thickness between old and young walls. However, the difference in labeling was less obvious with LM24 (see below), suggesting that the changes in labeling do not depend only on wall thickness.
- The LM25 antibody has a strong affinity for both XXXG and XXLG and a weak affinity for XLLG. Figure 1C shows a relatively homogeneous labeling across the meristem with this antibody. As indicated above, labeling with LM15 already indicated that XXXG was highly localized in the internal tissues.
- LM24, which mainly detects the XLLG epitope, strongly labels the organ boundaries and the L1 layer, in particular its outer walls and central zone (Fig. 1, B–D; Supplemental Figs. S1–S3). LM24 also labels the rib meristem.

In summary, our results on the wild-type SAM show specific distribution patterns of XyGs in the SAM, correlated with a number of basic meristem functions, including organ initiation (i.e. LM15 and LM24), meristem maintenance (i.e. LM24), and boundary formation (i.e. LM25 and LM24). Note that the higher signals of labeling in differentiated cells at meristem base could at least in part depend on the thickness of the walls.

Altered XyG Content in Meristems of *xxt1xxt2* and *xyl1-4* Mutants

To further investigate the role of XyGs in SAM function, we analyzed *xxt1xxt2* and *xyl1-4*, two mutants affected in enzymes with an opposite effect on XyG side chain branching (Faik et al., 2002; Minic et al., 2004). As indicated above, whereas XXT1 and XXT2

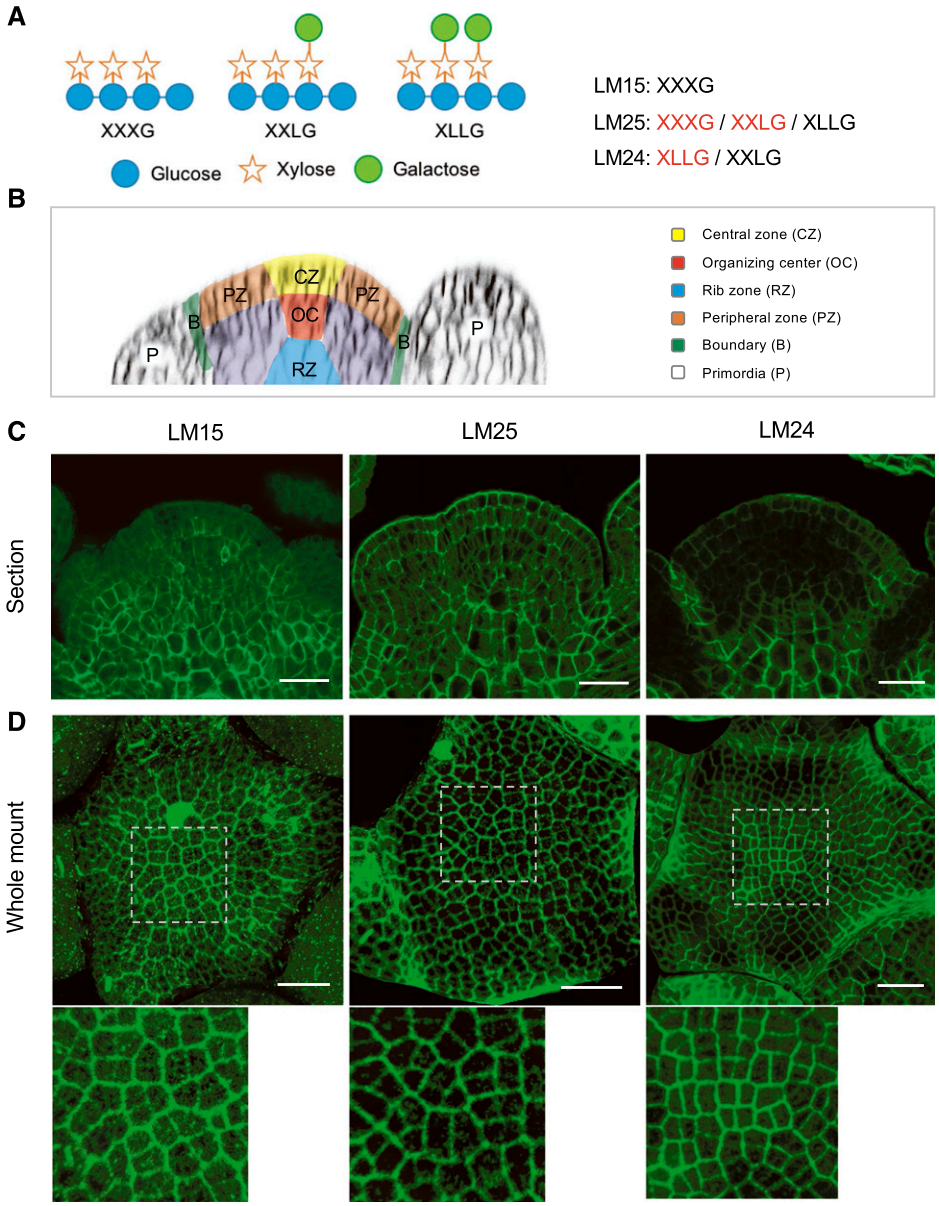

Figure 1. Differential distribution of xyloglucans (XyGs) in Arabidopsis wild-type shoot apices. A, Schematic structures of XyG subunits and specificity of XyG antibodies. Letters highlighted by red color mean higher affinity. B, Schematic structure of Arabidopsis SAM. C and D, Immunolocalization of XyGs in wild-type (Col) shoot apex sections (C) and whole mount tissues (D) labeled with LM15, LM25, and LM24 antibodies. Details are shown at bottom of (D). Scale bars = 20 μm.

are responsible for the addition of D-Xyl on the D-Glc backbone, this D-Xyl residue is removed by XYL1. As shown by in situ hybridization, all three genes are expressed at the meristem and show partially overlapping patterns (Supplemental Fig. S4). *XYL1* shows the highest expression in the young initia and flower buds. As reported by Yang et al. (2016), both *XXT1* and *XXT2* are mostly expressed in young primordia (see also Supplemental Fig. S4).

We then used the three antibodies mentioned above on the mutants. Although immunolabeling allows only semiquantitative analysis, we systematically found that LM15 labeling of XXXG slightly increases throughout the meristems of *xyl1-4* when compared with wild type (Figs. 1, C and D, and 2, A and B; Supplemental Figs. S1–S3). LM25 also shows increased labeling throughout the meristem in the mutant (Fig. 1, C and D, and 2, A and B; Supplemental Fig. S1–S3). This increase can in principle be explained by a change in wall thickness. However, this is not confirmed by the other antibodies. Indeed, LM24 labeling even indicates a slight reduction in XLLG mainly in the inner tissues of *xyl1-4* meristems (Figs. 1C and 2A; Supplemental Figs. S1 and S2). Interestingly, *xyl1-4* meristems show a lower signal with LM24 in the L1 of the central zone compared with wild type (Figs. 1, C and D, and 2, A and B; Supplemental Figs. S1–S3). As expected, there are no detectable XyGs in the cell walls of *xxt1xxt2* meristems (Fig. 2C; Supplemental Figs. S1 and S2; see Supplemental Fig. S2 for background controls).

For a more quantitative approach, we carried out an analysis of XyG composition by matrix assisted laser-desorption ionization time of flight mass spectrometry

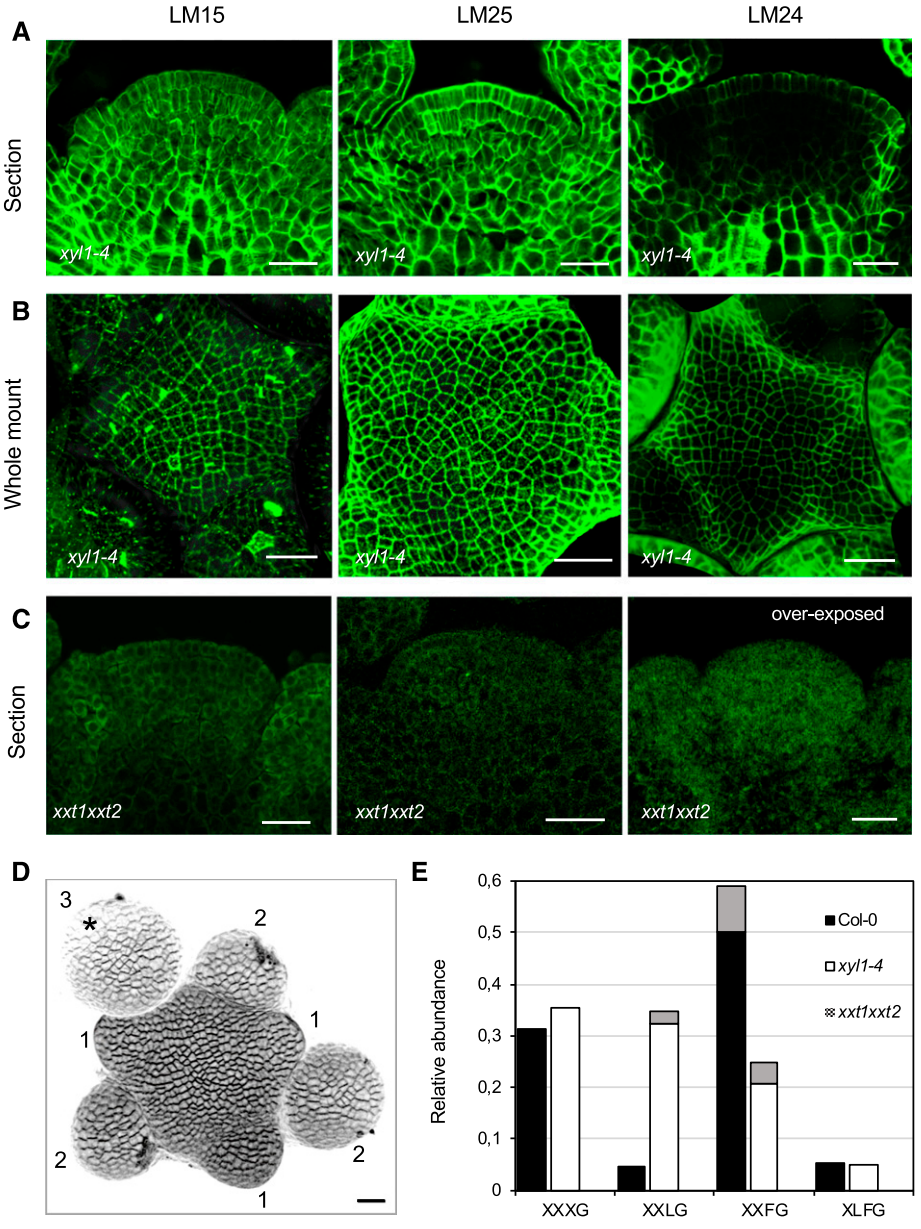

Figure 2. Altered distribution of XyGs in Arabidopsis XyG mutant shoot apices. A to C, Immunolocalization of XyGs in mutant backgrounds using LM15, LM25, and LM24 antibodies. Sections of *xyl1-4* shoot apices (A), whole mount labeling of *xyl1-4* (B), and sections of *xxt1xxt2* shoot apices (C) are shown. Scale bars = 20 μm. D, Three-dimensional reconstruction image of the shoot apices prepared for XyG composition analysis. The buds are numbered according to their developmental stages (Smyth et al., 1990). Asterisk marks the flower bud at stage 3, which was not included for the sampling. Scale bar = 20 μm. E, MALDI-TOF MS analysis of XyGs in wild-type, *xyl1-4*, and *xxt1xxt2* shoot apices. Gray areas of columns represent the proportion of acetylated subunits.

(MALDI-TOF MS). We dissected 50 meristems of each genotype, which included flower buds younger than stage 3 (Fig. 2D). The results are shown in the Figure 2E. As expected, we did not find any XyG in *xxt1xxt2* meristems. *xyl1-4* meristems show higher levels of XXLG and a slight increase in XXXG compared with the wild type, thus in line with the immunolabeling results. In addition, MALDI-TOF revealed a slight decrease in XLFG residues as well as a reduction in XXFG residues compared with the wild type. These changes in XyG fingerprint profiles in the XyG mutants are similar to those found in seedlings (Günl and Pauly, 2011), stems (Sampedro et al., 2010), and embryos (Sechet et al., 2016), suggesting that these enzymes broadly participate in regulating plant development. All together, these results demonstrate that XYL1 and XXT1/2 also regulate XyG composition in the SAM.

The *xxt1xxt2* Mutations Affect Cellulose Content as well as Pectin Methylation in the Meristem

Mutations affecting XyG composition can also lead to alterations of other wall components (Cavalier et al., 2008; Zabotina et al., 2012; Xiao et al., 2016). To test if this was also the case for the SAM, we carried out immunolabeling on wild-type and XyG mutant meristems using a range of antibodies. Pectin and its modifications have been implicated in meristem function (Peaucelle et al., 2008; Peaucelle et al., 2011). We found strong labeling of phragmoplasts in dividing cells using

the LM19 antibody, but we could not detect clear changes in the distribution of methylated (Fig. 3, A and B; Supplemental Fig. S5A) and de-methylated pectin (Fig. 3, C and D; Supplemental Fig. S5, B and C) in XyG mutant meristems using JIM7 and LM19 antibodies. We then further tested the distribution of cellulose, arabinan, xylan, arabinoxylan, and arabinogalactan in XyG deficient mutant meristems. Within the limitations of antibody specificities, we could not find any indication that the distribution of these wall components is perturbed in the mutants (Fig. 3E; Supplemental Fig. S5D and S6). Note that LM6 (anti-L-Arabinan), LM11 (antixylan/arabinoxylan), LM13 (anti (1,5)-arabinan), and LM14 (antiarabinogalactan) only showed labeling of cytoplasmic components (Supplemental Fig. S6), which could be due to the masking effect by other wall components. We noted a weak but reproducible labeling by LM11 of the walls in the central zone of *xxt1 xxt2*. This could reflect either a change in the abundance of the corresponding epitope or point at a reduced masking by other components (Supplemental Fig. S6C).

Because immunolabeling provides only semiquantitative information on absolute levels, we performed acid hydrolysis of the cell wall and High Pressure Anion-exchange Chromatography coupled with Pulsed Amperometric Detection (HPAEC-PAD) analysis using wild type and XyG mutant inflorescences to obtain whole monosaccharides profiles. The results presented in Figure 3, F–I, show that there are no dramatic changes in the composition of the walls of the *xyl1-4* mutant, in coherence with the immunolabeling data. By contrast, in *xxt1xxt2* a 22% decrease in cellulose content was found (Fig. 3F). Although, there is some variability in the measurements, it is important to note that a similar trend was found by Cavalier et al. (2008) and Xiao et al. (2016). In addition, a 12%

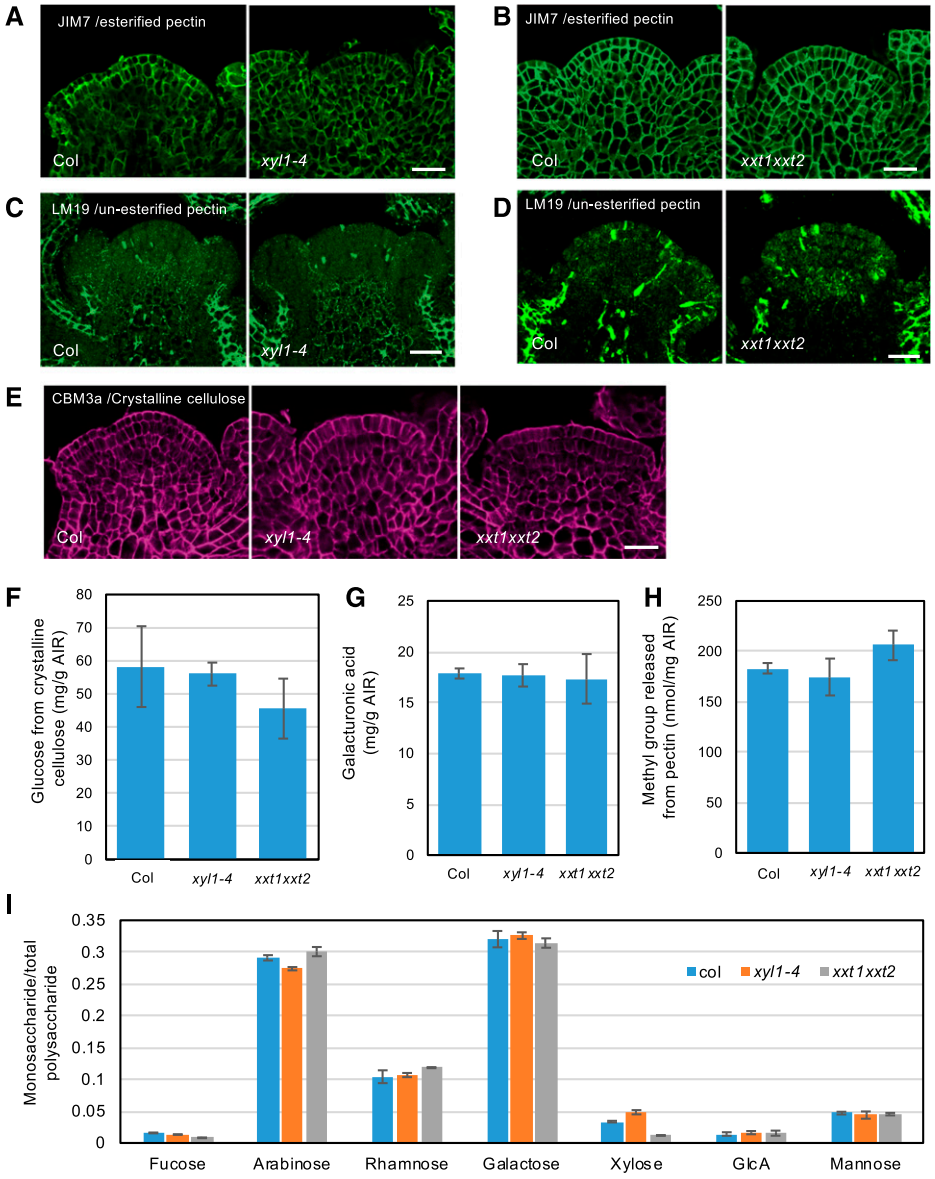

Figure 3. Distribution of other wall components in *xyl1-4* and *xxt1xxt2* SAM. A and B, Distribution of methyl-esterified pectin in *xyl1-4* (A) and *xxt1xxt2* (B) SAMs labeled with JIM7 antibody. C and D, Distribution of unesterified pectin in *xyl1-4* (C) and *xxt1xxt2* (D) SAMs labeled with LM19 antibody. E, Distribution of crystalline cellulose in *xyl1-4* and *xxt1xxt2* SAMs labeled with CBM3a antibody. Scale bars = 30 μm. F to I, HPAEC-PAD analysis of relative amounts of cellulose (F), homogalacturonan (G), methylesterified pectin (H), and other polysaccharides (I) in XyG mutant inflorescences. Results are shown as mean ± SD obtained from 3 replications.

increase in methylated pectin was found (Fig. 3, G–H). Finally, a prominent drop in Fuc (49%, mean value) and Xyl (65%, mean value) was observed in *xxt1xxt2* inflorescences, which is consistent with the absence of xyloglucans in this mutant (Fig. 3I). In conclusion, our results suggest that the severe reduction of XyG levels in *xxt1xxt2* alters cellulose levels and pectin methylation at the SAM, whereas the effects of *xyl1* are more limited.

Altered XyG Composition Affects Meristem Shape and Phyllotaxis

We next analyzed the *xyl1* and *xxt1xxt2* phenotypes. The *xyl1-4* mutant has smaller rosette leaves (Supplemental Fig. S7, A and B), a phenotype previously also described for *xxt1xxt2* (Park and Cosgrove, 2012; Xiao et al., 2016). Inflorescence stems of both mutants are not growing straight (Supplemental Fig. S7C; Xiao et al., 2016). In addition, we observed problems with phyllotaxis in both mutants as shown in Figure 4A. The *xyl1-4* mutant exhibits a more variable angle distribution when compared with the wild type, with an extra peak at 240° (Fig. 4, B and C). Perturbation in phyllotaxis was also observed in *xxt1xxt2* mutants but with different characteristics as the divergence angles in *xxt1xxt2* are often smaller than 137.5° (Fig. 4, B and C) and show a peak at 120°. This change in phyllotaxis could possibly be explained by a post-meristematic twisting of the cell files along the stem. However, we could not detect any evidence for this (Supplemental Fig. S8). It was therefore likely that the changes in phyllotaxis mainly occur at the meristem. To confirm this, we used 3D reconstructions from confocal images and measured successive angles between flower primordia and young flowers on the SAM as described in Figure 4D. The distribution of divergence angles on the SAM is significantly broader in both *xyl1-4* ($n = 6$ plants and 55 angles; $P < 0.05$, Kolmogorov-Smirnov test) and

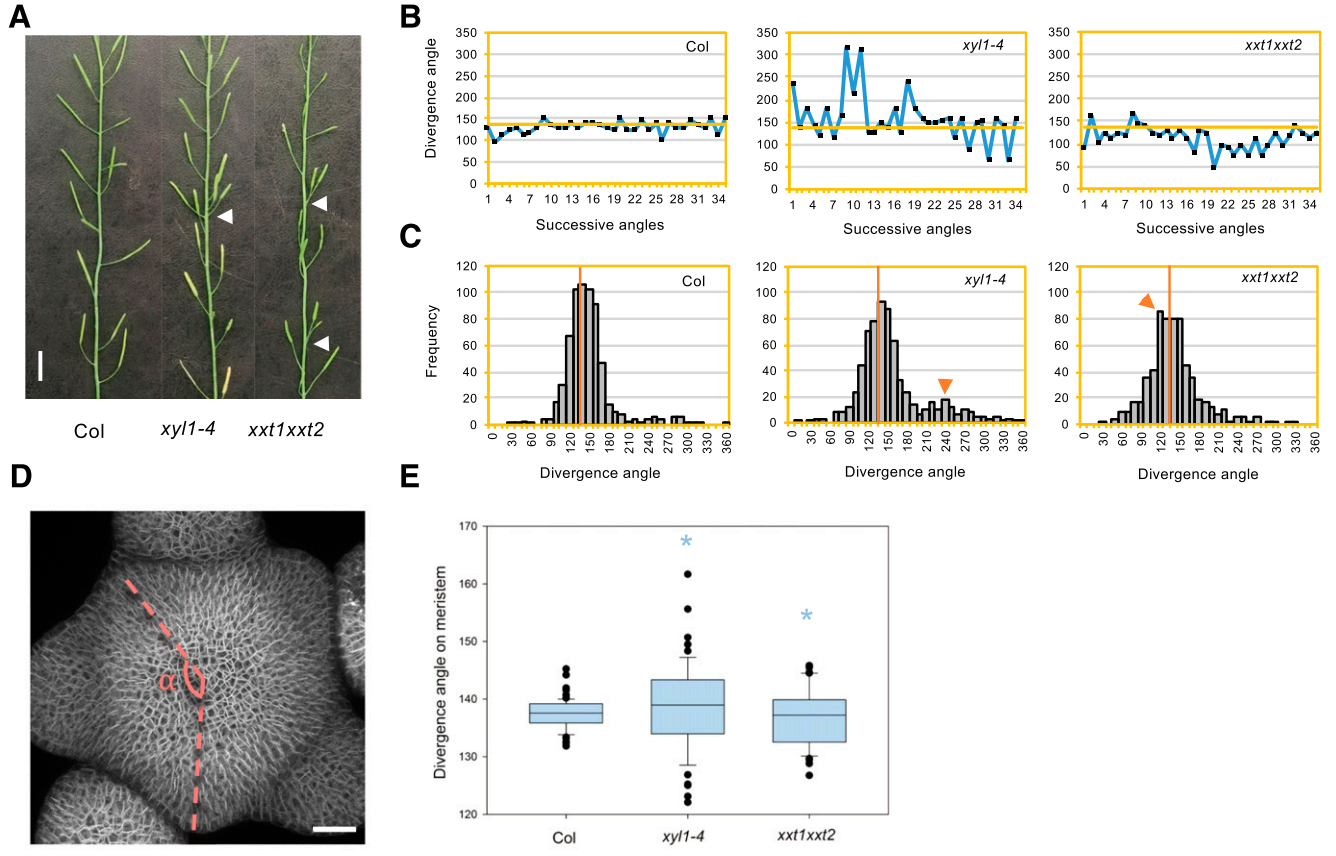

Figure 4. Phyllotactic phenotype of XyG mutants. A, Representative image showing perturbation of phyllotaxis (indicated by arrowhead) in *xyl1-4* and *xxt1xxt2* mutants. Scale bar = 1 cm. B, Representative distribution angles of siliques on the inflorescence stem of Col, *xyl1-4*, and *xxt1xxt2* plants. C, Distribution of divergence angles of siliques on the Col, *xyl1-4*, and *xxt1xxt2* inflorescence stems. Orange lines denote the position of a divergence angle of 137°. Orange arrowheads mark the abnormal angle peaks; $n = 649$ angles from 20 Col plants; $n = 683$ angles from 21 *xyl1-4* plants; $n = 635$ angles from 21 *xxt1xxt2* plants. D, Diagram showing the method to measure the divergence angles (α) between successive primordia on confocal images of live meristems. Scale bar = 20 μm. E, Primordia distribution angles on Col, *xyl1-4*, and *xxt1xxt2* meristems; $n = 67$ angles from 11 Col meristems; $n = 55$ angles from 6 *xyl1-4* meristems; $n = 46$ angles from 8 *xxt1xxt2* meristems. Asterisks denote statistically significant differences with wild type; $^*P < 0.05$, Kolmogorov-Smirnov test.

xxt1xxt2 (n = 8 plants and 46 angles; $P < 0.05$, Kolmogorov-Smirnov test) compared with Col-0 (n = 10 plants and 67 angles; Fig. 4E), showing that the organ initiation pattern is perturbed in both mutants.

The perturbed phyllotaxis goes along with changes in meristem shape and size. We used the radius (R) of the meristem to calculate meristem curvature (1/R, see also "Materials and Methods" for details). As shown in Figure 5, *xyl1-4* has a flat meristem (Fig. 5, A and D) when compared with the wild type. We then used MorphographX (Barbier de Reuille et al., 2015) for a more detailed quantitative analysis. This showed that average cell size is comparable with wild-type in *xyl1-4* (Fig. 5, A and B) and therefore is not correlated with these changes in overall geometry (Fig. 5, A and D). The meristem of *xxt1xxt2* is flatter and smaller than the wild-type (Fig. 5, A, C, and D). Cell size is not altered in the mutant (Fig. 5B), showing that reduced meristem size is correlated with reduced cell numbers. In conclusion, the phyllotactic defects observed in both XyG mutants are likely caused by perturbations in organ initiation at the meristematic level and correlate with changes in SAM size and shape.

Atomic Force Microscopy Indentation Does Not Reveal Any Difference in Wall Young's Modulus between Mutants and Wild Type

Changes in geometry and morphogenesis generally result from changes in growth patterns, which in turn

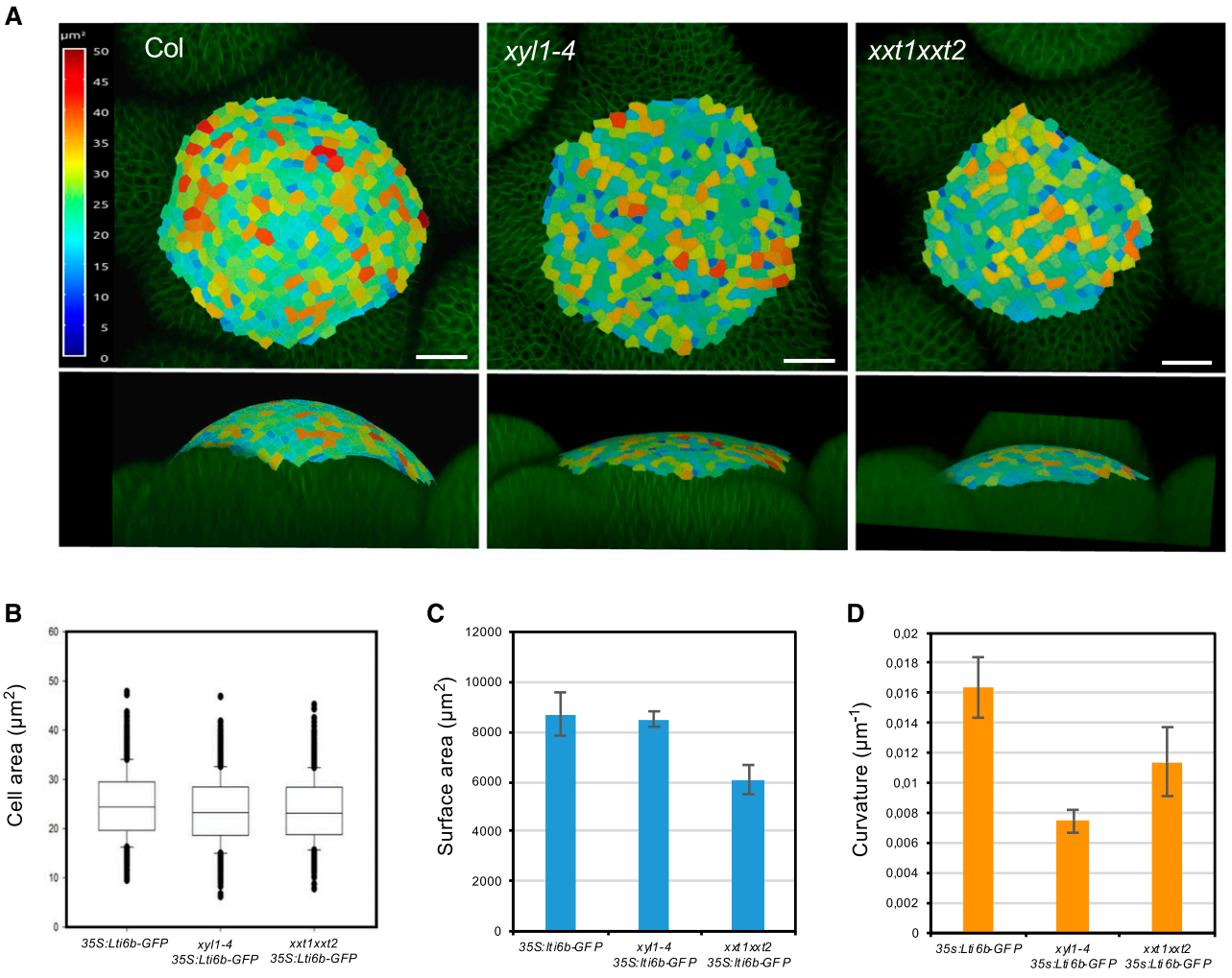

Figure 5. Meristem size and geometry of wild-type and XyG mutants. A, Overview of meristem size and geometry. Top, distribution map of cell area on Col and XyG mutant SAMs. Bottom, meristem curvature. All plants harbored the plasma membrane marker (*35S:Lti6b-GFP*). Images were postprocessed using the MorphoGraphX software. B, Cell area on meristem surface; n = 1409 cells from 4 meristems of *35S:Lti6b-GFP*; n = 1469 cells from 4 meristems of *xyl1-4 35S:Lti6b-GFP*; n = 1028 cells from 4 meristems of *xxt1xxt2 35S:Lti6b-GFP*. Box plots display the interquartile range, split by the median; whiskers indicate the total range; outliers are plotted as individual points. C, Surface area of Col and XyG mutant meristems calculated from (B). D, Surface curvature of Col and XyGs mutant meristems; n = 11 for Col meristems; n = 10 for *xyl1-4* meristems; n = 8 for *xxt1xxt2* meristems. Mean values are represented with SD in (C) and (D).

largely depend on wall stiffness and the degree of anisotropy. We therefore investigated the mechanical properties of the walls in both mutants using atomic force microscopy (AFM)–based nano-indentation on *xyl1-4* and *xxt1xxt2* mutant meristems. We used a silica spherical tip mounted on a silicon cantilever with a nominal force constant of 42 N/m, and a radius of 400 nm (Bovio et al., 2019; see also "Material and Methods"). The applied force was of 1 μN, a force corresponding to 100–200 nm indentation, in order to indent the cell wall only (Milani et al., 2011; Tvergaard and Needleman, 2018). Unexpectedly, as shown in Figure 6, we did not find differences between wild type, *xyl1-4* and *xxt1xxt2* at least by applying forces in anticlinal direction on the SAM.

Microtubule Alignment and Dynamics Are Perturbed in XyG Mutant Meristems

Previous studies have suggested that modified XyG contents can affect cell wall anisotropy and the arrangements of cellulose microfibrils (Xiao et al., 2016). Because microfibril orientations depend on the cortical microtubules (CMTs) guiding the cellulose synthase complexes, we next compared CMT dynamics in wild type and mutants. For this purpose, we introgressed the microtubule reporter construct *p35S:GFP-MBD* into *xyl1-4* and *xxt1xxt2* mutants. Because the GFP-signal was silenced in the *xxt1xxt2* meristem, we used *pPDF1:mCitrine-MBD* to visualize the microtubules in that mutant. The results are shown in Figure 7. Confocal imaging revealed that microtubules were less aligned between cells at the meristem in both mutants compared with the wild type (Fig. 7, A–C; Supplemental Fig. S9 for in vivo images), reflecting a reduced coordination of CMTs at the tissue level. These differences were more pronounced in *xyl1-4* ($P < 0.001$, Kolmogorov-Smirnov test) and relatively small but significant in *xxt1xxt2* ($P < 0.05$, Kolmogorov-Smirnov test). In *xyl1-4*, CMTs are less well-aligned than in the wild type and in particular show a decrease in angles between 75° and 90° relative to the meristem radius. In *xxt1xxt2*, the difference mainly exists at the portion of around 90°. Interestingly, this seemed to result from different effects at the cellular level. Although the differences are subtle, CMTs are significantly more isotropic in individual cells of *xyl1-4* meristems when compared with the wild type (Fig. 7D, $P < 0.001$, Kolmogorov-Smirnov test), whereas they are more anisotropic in the *xxt1xxt2* mutant meristem (Fig. 7E, $P < 0.001$, Kolmogorov-Smirnov test; Supplemental Fig. S9).

Microtubule Dynamics May Partially Compensate the XyG Defects in Mutant SAMs

There is convincing evidence that CMTs organize in function of mechanical constraints (Hamant et al., 2008; Landrein and Hamant, 2013). The changes in CMT organization observed in the XyG mutants could be due to an altered capacity of the cytoskeleton to reorganize upon mechanical constraints. We tested this capacity in the XyG mutants by performing cell ablations on dissected meristems of plants grown on soil. This causes specific, circumferential rearrangements of the CMT arrays in the cells around the wound. Under our experimental conditions, circumferential microtubule arrays surrounding the wounding start to form 2 h after ablation in wild-type meristems (Fig. 8, A and D). We quantified the microtubule rotation angles after ablation in both XyG mutants and did not find any significant delay in CMT rearrangements when compared with wild type (Fig. 8). These results show that in *xyl1-4* and *xxt1xxt2*, cells have the capacity to perceive exogenous forces and are perfectly able to respond. We therefore hypothesized that the observed changes in CMT anisotropy in the XyG mutants might be due to an active response of the cytoskeleton to altered wall composition. If this is true, perturbing this response could lead to more severe phenotypes in *xxt1xxt2* or *xyl1-4* backgrounds.

To test this hypothesis, we used the *botero* mutant (*bot1/ ktn1*), perturbed in KATANIN, a microtubule severing protein required for microtubule alignment, and introduced the mutation in *xyl1-4* and *xxt1xxt2*. The wild-type of Col-0 and Ws have comparable shape and curvature (Uyttewaal et al., 2012; Gruel et al., 2016; Fig. 5D). As shown in Figure 9, the *xyl1-4 bot1-7* double mutant SAMs have striking concave meristems with a bumpy surface SAM, a phenotype which is much enhanced compared with single mutants (Fig. 9A). In certain individuals, the meristem center was almost hidden between the irregular outgrowths at the surface of the meristem periphery. Several continuous bumps along the orthogonal cutting planes indicated

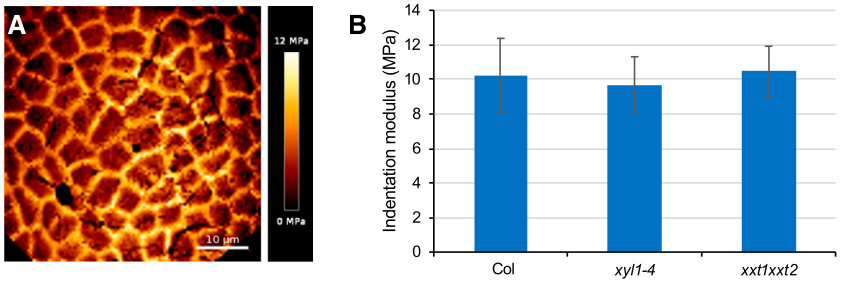

Figure 6. Young's modulus of cell walls from Col, *xyl1-4* and *xxt1xxt2* SAMs. A, Representative map of indentation moduli on Col meristem surface. B, Quantification of Indentation modulus of Col, *xyl1-4*, and *xxt1xxt2* SAMs; $n = 6$ for Col meristems; $n = 7$ for *xyl1-4* meristems; $n = 6$ for *xxt1xxt2* meristems. Mean values are shown with SD.

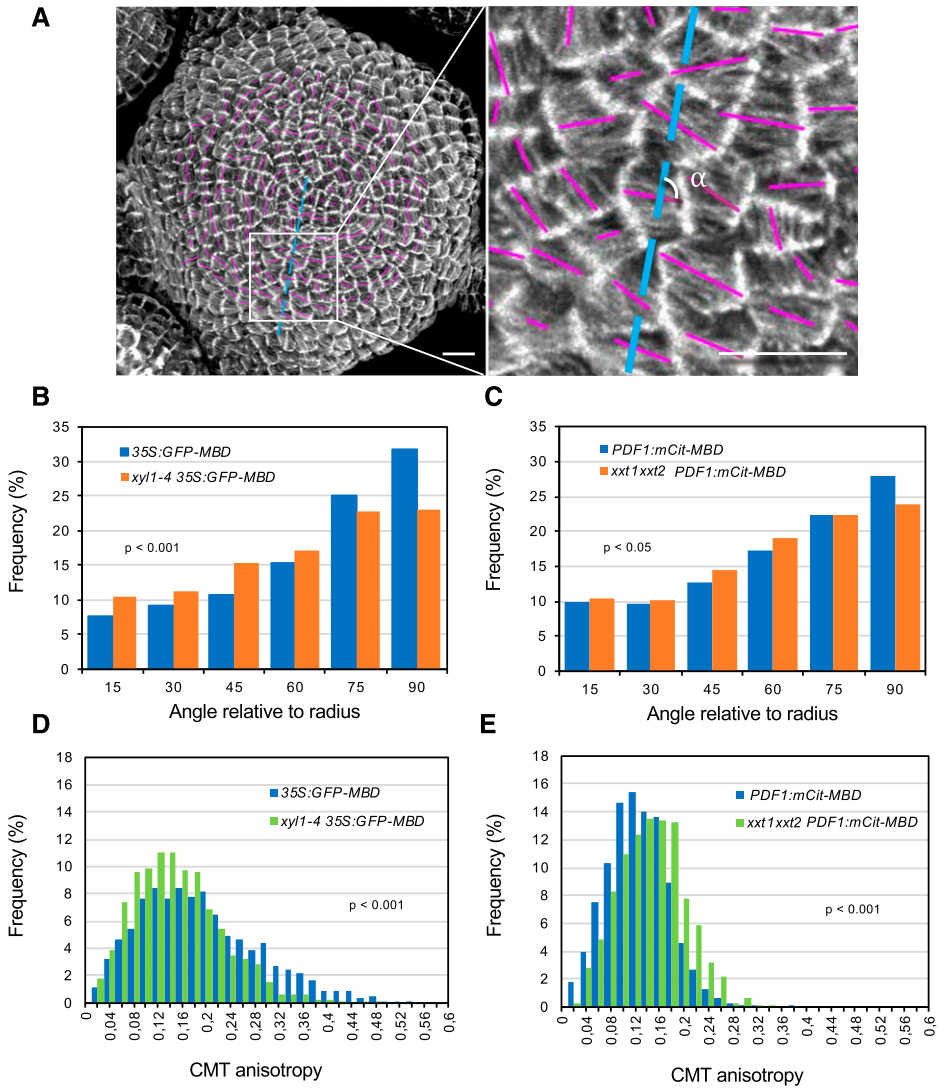

Figure 7. Microtubule patterning on wild-type and XyG mutant SAMs. A, Representative microtubule patterning on *35S:GFP-MBD* SAM. The orientation and length of magenta bars represent average microtubule orientation and degree of anisotropy in a single cell, respectively. Blue lines represent the radius of meristem. Details are enlarged at right. The α indicates the angle relative to radius. Scale bars = 10 μm. B and C, Quantifications of CMT orientation relative to the radius of *xyl1-4* (B) and *xxt1xxt2* (C) SAMs. D and E, Quantifications of CMT anisotropy in *xyl1-4* (D) and *xxt1xxt2* € SAMs. Statistic data in (B–E) was calculated from n = 1345 cells of 5 meristems of *35S:GFP-MBD*, n = 1522 cells of 5 meristems of *xyl1-4 35S:GFP-MBD*, n = 1203 cells of 5 meristems of *PDF1:mCitrine-MBD*, and n = 998 cells of 5 meristems of *xxt1xxt2 PDF1:mCitrine-MBD*. *P*-values are calculated based on Kolmogorov-Smirnov test in (B–E). See also Supplemental Figure S9 for more details of CMT organization.

that the coordination of organ growth and separation was affected (Fig. 9B). Consistent with this observation, we observed a dramatic change in phyllotaxis in *xyl1-4bot1-7* double mutants (Fig. 9C–E) compared with wild type and *bot1-7* single mutants grown under the same growth condition (Landrein et al., 2015). In view of the irregular surface of the meristems, it was sometimes difficult to establish the precise sequence of organ initiation at the meristem in the double mutant. Therefore, we cannot exclude the possibility that the severely perturbed phyllotaxis results from both meristematic and post-meristematic events. The cross between *xxt1xxt2* and *ktn1* resulted in even more extreme phenotypes. When we analyzed the offspring of mother plants that were homozygous for *xxt1* and *ktn1* while heterozygous for *xxt2*, we were only able to retrieve four triple mutants in an offspring of 147 plants. These mutants were very small and did not develop beyond the seedling stage (Fig. 10). In conclusion, our results point at negative epistatic interactions, showing that the control of CMT dynamics by KTN becomes vital when XyGs are perturbed or absent.

DISCUSSION

The precise function of XyGs in development has remained controversial. In a previous study, we showed that genes encoding XyGs modifying enzymes like the xyloglucan endotransglucosylases/hydrolases are highly expressed and show specific expression patterns at the meristem, suggesting an important role for XyGs during morphogenesis (Armezzani et al., 2018). Here we explored the role of these components further, and show that specific XyG residues accumulate in different functional domains of the SAM. The organ boundaries and the meristem summit, for example, are characterized by higher LM24 labeling, which probably reflects an increase in XLLG and XXLG subunits. What this precisely implies has yet to be determined, but it should be noted that these domains are characterized

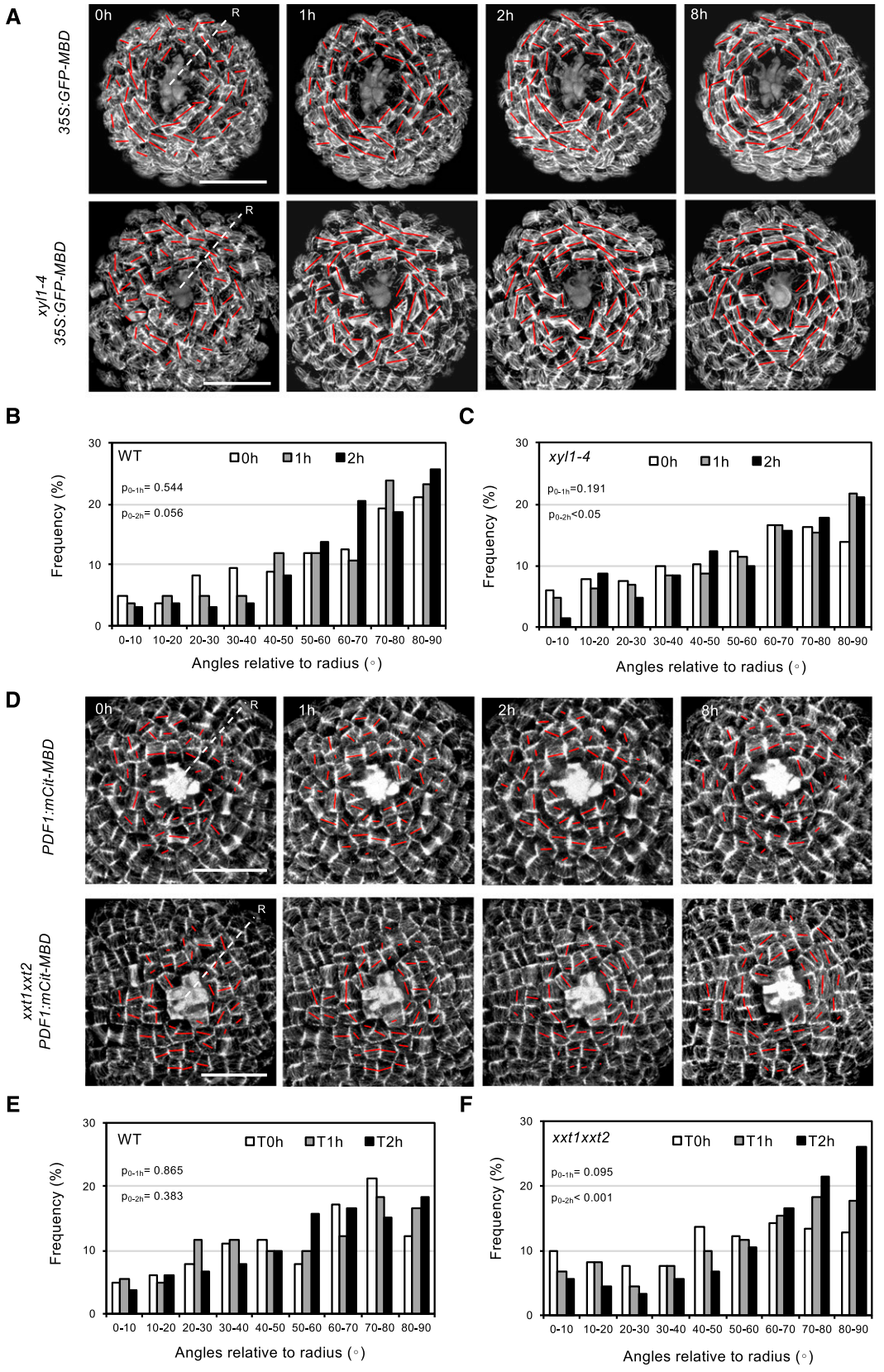

Figure 8. CMT reactions to mechanical perturbation in wild-type, *xyl1-4*, and *xxt1xxt2* SAMs. A, Time series of CMT patterning in *35S:GFP-MBD* (wild type [WT]) and *xyl1-4 35S:GFP-MBD* SAMs after laser ablation at the meristem center. The orientation and

by slowly growing cells (Kwiatkowska and Dumais, 2003; Kwiatkowska and Routier-Kierzkowska, 2009). The stiffness of the walls at the boundary has not been studied, but the cells at the meristem summit are slightly more rigid and might be in a particular mechanical, hyperelastic state beyond their linear range of elastic deformation (Kierzkowski et al., 2012; Milani et al., 2014).

The changes in meristem shape are accompanied by modifications in phyllotaxis in both mutants, which can be, at least in part, traced back to early events during organ positioning. There are several possible explanations for this. First, organ outgrowth could be partially impaired, or more irregular, causing young primordia to grow at more variable rates. Such abnormal growth patterns could destabilize the phyllotactic patterns, for example when an organ grows out more quickly than its predecessor. This type of anomaly, leading to permutations of the positions of successive organs along the stem, has been described for the *ahp6* mutant for example, which is impaired in cytokinin signaling (Besnard et al., 2014). Alternatively, the organ positioning process itself could be modified. As indicated above, organ initiation is caused by the local accumulation of auxin. This accumulation depends on membrane associated auxin transporters of the PIN-FORMED (PIN) family, which often show a polar localization. Several studies have pointed at an important role for cell wall components in this polar distribution (Boutté et al., 2006; Heisler et al., 2010; Braybrook and Peaucelle, 2013). Removal of the cell wall during protoplasting leads to a redistribution of PIN at the cell membrane (Boutté et al., 2006). Certain mutants in cellulose synthase show altered PIN localization in the root (Feraru et al., 2011). It is therefore possible that the modified cell wall composition in the XyG mutants perturbs phyllotaxis via modified patterns of auxin transport.

The rather mild phenotypes observed after severe changes in such a major wall component remain surprising. Several authors have suggested that this is due to the compensatory action of other cell wall components. In particular pectin has been proposed as a possible source of such a compensation. Although the mutations do not affect the total amount of pectin at the meristem, we did identify a 12% increase in methylesterification in *xxt1xxt2* when compared with wild type, despite the fact that we did not detect changes in the overall distribution of the different pectin forms using JIM7 and LM19 antibodies. If we suppose that pectins are the main source for compensation, a 12% increase in pectin methylesterification would then be sufficient. Indeed, the replacement of a carboxyl end with a methyl group changes pectin properties, and potentially affects the dimerization of homogalacturonan mediated by the interaction of Ca^{2+} with unmethylated stretches of GalUA. Note that we did not observe any significant change in the Young's modulus of the walls, but it remains to be seen if the observed increase in methylesterification would be sufficient to compensate for the absence XyGs.

The results also point at a link between altered XyG content and different aspects of cellulose deposition. The *xxt1xxt2* mutant has a decreased amount of cellulose, whereas the meristems of both *xxt1xxt2* and *xyl1* have modified microtubule dynamics, suggesting altered microfibril deposition as was also reported for hypocotyls (Xiao et al., 2016). In addition the phenotypes are severely enhanced when the XyG mutants are combined with *bot1/ktn1*, impaired in microtubule severing. Therefore, the cytoskeleton seems to compensate at least in part for the loss of XyGs. Indeed, in the absence of XyGs, *bot1/ktn1,* normally able to produce fertile plants, is not able to develop beyond the seedling stage. In addition, combining mutation in *bot1/ktn1* with *xyl1* dramatically increases defects in phyllotaxis and meristem geometry. The altered dynamics of the microtubules most clearly seen in the meristem of *xyl1* could be due to a reduced or altered capacity of the cytoskeleton to rearrange when cell wall composition is changed as was suggested by Xiao et al. (2016). However, the ablation experiments suggest that microtubule dynamics are intact in the mutants. It is therefore reasonable to propose that the altered dynamics of microtubules observed in the mutants reflect some type of active regulation aimed at compensating for the changes in XyG composition. How such a compensation would work is not easy to predict. Part of the answer might come from a role of KTN controlled CMT dynamics in regulating the amount of cellulose, as cellulose levels drop by 20% in stems of the *bot1/ktn1* mutant (Burk et al., 2001). Our own unpublished results even show a 40% drop in the shoot apex (F. Zhao, J. Sechet, and J. Traas, unpublished data). Maintaining the cellulose levels might become critical when XyGs are modified.

The reduced cellulose levels in *bot1/ktn1* raise in turn a number of questions. First, it is not clear why changes in microtubule severing would inhibit the deposition of cellulose so dramatically. Second, cellulose is supposed to contribute significantly to wall stiffness. However, we didn't measure any important change in the elastic modulus using AFM in *bot1/ktn1*

Figure 8. (*Continued.*)
the length of the red bar represent average CMT orientation and degree of CMT anisotropy respectively at cellular level. B and C, Quantification of CMT orientation angles relative to radius of wild type (B) and *xyl1-4* (C) SAMs, 1 and 2 h after laser ablation; n = 167 cells from 4 wild-type meristems and n = 204 cells from 4 *xyl1-4* meristems. D, Time series of CMT patterning on *pPDF1:mCitrine-MBD* (wild type) and *xxt1xxt2 pPDF1:mCitrine-MBD* SAMs after laser ablation at the meristem center. E and F, Quantification of CMT orientation angles relative to the SAM radius of wild type (E) and *xxt1xxt2* (F) SAMs, 1 and 2 h after laser ablation; n = 164 cells from 4 wild-type meristems and n = 181 cells from 4 *xxt1xxt2* meristems. 'R' in (A and D) represents radius of meristem. *P*-values are calculated based on Kolmogorov-Smirnov test. Scale bars = 20 μm.

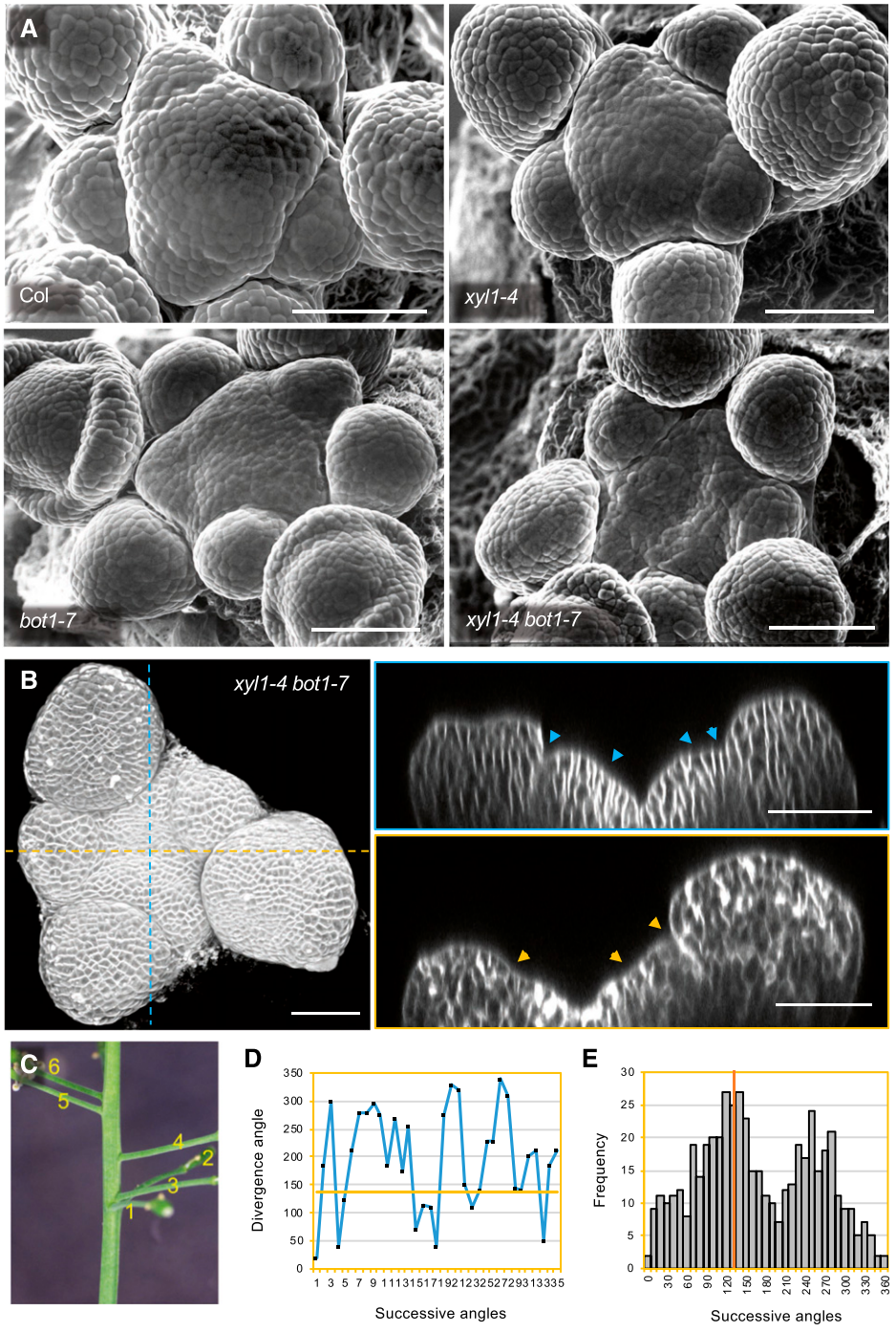

Figure 9. Phenotype of *xyl1-4 bot1-7*. A, Scanning Electron Microscope (SEM) images of Col, *xyl1-4*, *bot1-7*, and *xyl1-4 bot1-7* SAMs. B, Three dimensional reconstruction (left) and orthogonal view (right) of confocal image of *xyl1-4 bot1-7* meristem. The arrowheads mark the points with negative curvatures on meristem surface, which are proposed to be organ boundaries. Scale bars = 50 μm (A and B). C, Representative image of silique distribution on *xyl1-4 bot1-7* stem. Numbers denote the silique positions from bottom to top (old to young). D, Representative silique distribution angles on the inflorescence stem of *xyl1-4 bot1-7*. E, Distribution of divergence angles of siliques on the *xyl1-4 bot1-7* inflorescence stems. Orange line denotes the position of angle around 137°; n = 504 angles from 10 plants.

(Uyttewaal et al., 2012; F. Zhao, S. Bovio, F. Monéger, and J. Traas, unpublished data). Although this needs to be further confirmed using other approaches (e.g. larger indentations on plasmolyzed cells), this could suggest that other components compensate for the potential reduction in stiffness due to the loss in cellulose. XyGs are somehow essential in this context, as their presence is absolutely required when KTN is impaired.

In conclusion, XyGs have a significant role in patterning at the shoot apical meristem. This could be due to a direct role of XyG composition in coordinating growth rates and directions, although indirect effects on cell polarity and auxin transport might also be involved. We also find that XyG composition can at least in part compensate for impaired cellulose deposition and vice versa. How this precisely works remains to be elucidated, but the results again illustrate the extraordinary capacity of plant cells to maintain and adapt the properties of their walls to guarantee robust development.

A

B

	xxt1/xxt2/ktn1	number of plants	% of genotypes
genotypes	ho/ho/ho	4	2,7
	ho/he/ho	74	50,3
	ho/wt/ho	69	46,9
	total	147	

Figure 10. Phenotype of a triple mutant *xxt1xxt2ktn1*. A, Phenotype of representative Col-0, *xxt1ktn1*, and *xxt1xxt2ktn1* plants grown in vitro for 3 weeks. Scale bar = 1 mm. B, Analysis of the progeny a *xxt1−/− xxt2+/− ktn−/−* plant. Among 147 plants, we identified 4 triple mutants.

MATERIALS AND METHODS

Plant Materials and Culture Conditions

Arabidopsis (*Arabidopsis thaliana*) Col-0 and Ws-2 ecotype plants were used as wild type. All mutants and marker lines used in this study have been described previously: *xxt1xxt2* (Col-0; Cavalier et al., 2008), *xyl1-4* (Col-0; Sechet et al., 2016), *bot1-7* (Ws-2; Sassi et al., 2014), *ktn1*(*SAIL_343_D12*; Lin et al., 2013), *35S:GFP-MBD* (Hamant et al., 2008), *35S:GFP-Lti6b* (Sassi et al., 2014), and *PDF1:mCitrine-MBD* (Stanislas et al., 2018). To obtain *xyl1-4 bot1-7* double homozygous plant, the plants were selfed after a first cross and homozygous *bot1-7*/heterozygous *xyl1* plants were selected in the third generation. The other materials were generated by crossing and subsequently confirmed by genotyping. Plants were grown on soil under long-day condition (16/8 h light period, using light-emitting diodes, 150 $\mu Em^{-2}s^{-1}$; 60% humidity and 20–22°C day temperature). For confocal and time-lapse imaging, shoot apices were dissected and cultured in vitro on apex culture medium (ACM) as described previously (Sassi et al., 2014).

Immunolocalization of Cell Wall Components

Inflorescence meristems were infiltrated in the formaldehyde-acetic acid fixative (3.7% [w/v] formaldehyde, 50% [v/v] ethanol, and 10% [v/v] acetic acid) under vacuum for 5 min and left in this solution overnight at 4°C. Paraffin embedding sectioning was carried out according to Zhao et al. (2017). Sections of wild type and mutant specimens were put on the same slide, then deparaffinized in Histo-Clear and rehydrated in a series of ethanol solutions, followed by treatment with membrane permeabilization solution (10% [v/v] dimethyl sulfoxide; 3% [v/v] Nonidet P-40) for 1 h. After being washed in 1× phosphate buffered saline (PBS) buffer (pH 7.0), the slides were incubated with primary antibodies: anticrystalline cellulose (Plant Probes, CBM3a [1:100]), antihomogalacturonan (Plant Probes, JIM7 [1:80] and LM19 [1:100]), anti-xyloglucan (Plant Probes, LM15 [1:100], LM24[1:200] and LM25[1:100]), anti-arabinan (Plant Probes, LM6 [1:100] and LM13 [1:50]), antixylan/arabinoxylan (Plant Probes, LM11[1:100]), and antiarabinogalactan (Plant Probes, LM14 [1:100]) in 1% (w/v) bovine serum albumin/PBS buffer (pH 7.0) overnight at 4°C and then the corresponding secondary antibodies: antirat IgG (Alexa Fluor 488 conjugated, Molecular Probes A21210 [1:100] and Dylight 550 Invitrogen SA5-10027 [1:100]), IgM (Dylight 488 conjugated, Abcam ab96963 [1:125]), and anti-His tag (Alexa Fluor 555 conjugated, Thermo Fisher MA1-21315-A555 [1:200]) for 3 h at 37°C. After being washed in PBS buffer (pH 7.0), the slides were observed in a Zeiss LSM 700 laser-scanning confocal microscope. To better detect XyG and cellulose signals, slides were treated with 0.1% (w/v) pectolyase (Sigma, P5936) in citric acid-sodium phosphate buffer (0.2 M Na_2HPO_4, 0.1 M citric acid [pH 4.8]) for 45 min before antibody incubation.

For whole mount immunolocalization, the method was set up based on Rozier et al. (2014). Briefly, dissected shoot apices were fixed in formaldehyde-acetic acid under vacuum for 1 h. After dehydration and rehydration in a series of ethanol solutions, the shoot apices were digested in a solution containing 0.1% (w/v) pectolyase and 0.1% (w/v) pectinase (with citric acid-sodium phosphate buffer [pH 4.8]) for 1 h at room temperature. The digestion time was optimized to keep optimal meristem integrity, as at longer treatments the tissues became extremely fragile. After membrane permeabilization as described above and being washed in 50 mM PIPES, 5 mM EGTA, 5 mM $MgSO_4$, pH 7.0, the shoot apices were incubated with primary antixyloglucan antibodies in 3% (w/v) bovine serum albumin/0.1% (v/v) triton/microtubule stabilizing buffer buffer overnight at 4°C followed by the corresponding secondary antibodies for 3 h at 37°C. After being washed with buffer, the apices were mounted vertically in Murashige and Skoog medium. Image were taken with a Zeiss LSM700 laser-scanning confocal microscope equipped with water immersion objectives (W N-Achroplan 40×/0.75 M27). All the details of cell wall antibodies and references referred to can be found on this Web site: http://www.plants.leeds.ac.uk/pk/pdf/JPKab05.pdf.

RNA in Situ Hybridization

RNA in situ hybridization on sections was performed according to (Armezzani et al., 2018) using digoxin-labeled *XYL1* (2924 bp, primers: 5`- ACC ATAAGCTAAAGAGGGTTCG and 5`- TAATACGACTCACTATAGGG GAA ATGGAGAAGAACAAAACATTACC), *XXT1* (938bp, primers: 5`-ATTCTG GGCTAAGCTTCCGTTG and 5`-TAATACGACTCACTATAGGG CTCCAT ACACGACTCCAC), and *XXT2* (538bp, primers: 5`-ATGATTGAGAGGTGT TTAGGAGC and 5`- TAATACGACTCACTATAGGG AGCCATCTCTGCATC GAG) probes from amplified PCR products (prepared according to Rozier et al., 2014). Images were taken with Zeiss Axio imager 2 microscope equipped with EC Plan-Neofluar 20×/0.5 objective.

Cell Wall Composition Analyses

To analyze the XyG contents on SAM following the oligosaccharide fingerprinting set up by Lerouxel et al., (2002), 50 shoot apices were dissected and kept in ethanol. After ethanol removal, XyG oligosaccharides were generated by treating samples with endoglucanase in 50 mM sodium acetate buffer, pH 5,

overnight at 37°C. MALDI-TOF mass spectrometry of the XyG oligosaccharides was recorded with a MALDI/TOF Bruker Reflex III using super-DHB (9:1 mixture of 2,5-dihydroxy-benzoic acid and 2-hydroxy-5- methoxy-benzoic acid; Sigma-Aldrich, sigmaaldrich.com) as matrix.

For whole cell wall component measurement, around 0.3 g fresh inflorescences were collected for analysis and fixed in 96% (v/v) ethanol. After grinding in ethanol, they were incubated for 30 min at 70°C. The pellet was then washed twice with 96% (v/v) ethanol and twice with acetone. The remaining pellet is called alcohol insoluble residues (AIR) and was dried in a fume hood overnight at room temperature.

For pectin measurement, saponification of the AIR (3 mg) was performed in triplicates with 0.05 M NaOH. The supernatant containing methyl ester released from the cell wall was then separated from the pellet with polysaccharides. Pectins were extracted from the pellet with 1% (w/v) ammonium oxalate at 80°C for 2 h as described (Krupková et al., 2007; Mouille et al., 2007; Neumetzler et al., 2012). GalUA was then quantified by colorimetry using meta-hydroxydiphenyl-sulfuric acid method as described (Blumenkrantz and Asboe-Hansen, 1973). Methyl ester was quantified from NaOH supernatant with a colorimetric assay using enzymatic oxidation of methanol (Klavons and Bennett, 1986).

The monosaccharide composition of the noncellulosic fraction was determined by hydrolysis of 100 μg AIR with 2 M TFA for 1 h at 120°C. After cooling and centrifugation, the supernatant was dried under a vacuum, resuspended in 200 μL of water and retained for analysis. To obtain the Glc content of the crystalline cellulose fraction, the TFA-insoluble pellet was further hydrolyzed with 72% (v/v) sulfuric acid for 1 h at room temperature. The sulfuric acid was then diluted to 1 M with water, and the samples incubated at 100°C for 3 h. All samples were filtered using a 20-μm filter caps and quantified by HPAEC-PAD on a Dionex ICS-5000 instrument (ThermoFisher Scientific) as described (Sechet et al., 2018).

Phenotypic Analysis (Phyllotaxy, Meristem Size, and Geometry Measurement)

The phyllotactic patterns were measured as described previously (Besnard et al., 2014). Cell size in the SAMs was obtained by using MorphoGraphX software according to the guideline (https://www.mpipz.mpg.de/MorphoGraphX/help). Only the cells within the organ boundaries were taken into account. The organ boundaries were defined as the regions with negative Gaussian curvature. Meristem size (surface area) was calculated by summing up all the cell areas per meristem. To calculate meristem curvature, confocal stacks were viewed as two independent orthogonal planes by using orthogonal views function in Fiji software (https://fiji.sc). The radius of meristem was evaluated by drawing a circle tangential to the inner surface of meristem summit. The radius of the circle was taken as the meristem radius (R). The meristem curvature was then calculated as 1/R. To decrease the bias of the measurement, we averaged the curvature value obtained from two orthogonal planes mentioned above on a single meristem. All the data were processed by SigmaPlot and Microsoft Excel software.

Live Imaging and Microscopy

For live imaging, dissected meristems were visualized using a membrane marker (*GFP-Lti6b*) under control of an appropriate promoter, or stained with propidium iodide. Samples were examined in a Zeiss LSM 700 laser-scanning confocal microscope equipped with water immersion objectives (W Plan-Apochromat 40×/1.0 differential interference contrast or W N-Achroplan 40×/0.75 M27). For scanning electron microscopy, freshly dissected meristems were observed with a HIROX SH-3000 tabletop microscope equipped −20°C and an accelerating voltage of 5 kV.

Image Processing and Analyses

Fiji software was used for two dimensional confocal image analysis. For 3D image processing, the Zeiss ZEN2 software was used to make a 3D maximum or transparent projection of the signals on meristem. MorphoGraphX software was used to reconstruct the outer meristem surface. To quantify cortical microtubule signals, the images were processed and analyzed according to Verger et al. (2018). More specifically, we first projected epidermal CMT signals and cell contours using MorphoGraphx and then used Fiji plugin MorphoLibJ (Legland et al., 2016) to segment the cells and define a region of interest (ROI). Finally, we used Fibril tool (Boudaoud et al., 2014) to quantify CMT orientation and anisotropy. The distribution of CMT orientation and anisotropy was plotted using Excel software. The significance of the differences in CMT distribution between wild type and mutant was evaluated by Kolmogorov-Smirnov test using SPSS software.

AFM

To prevent vibrations, cleanly dissected meristems were fixed vertically on a 60-mm petri dish (Falcon 60 mm × 15 mm, Corning Ref. 351007) by using biocompatible glue Thin Pour (Reprorubber, Flexbar Ref 16135). AFM experiments were performed on a stand-alone JPK Nanowizard III microscope, driven by a JPK Nanowizard software 6.0. The acquisitions were done using the Quantitative Imaging mode. The experiments have been performed in liquid ACM at room temperature: liquid ACM was added into the petri dish to rehydrate meristems around 1 h before the beginning of the measurements. We used a silica spherical tip with a nominal radius of 400 nm (Special Development SD-sphere-NCH, Nanosensors) mounted on a silicon cantilever with a nominal force constant of 42 N/m. Scan size was generally of 50 μm with pixel size of 500 nm. The applied force trigger was of 1 μN, a force corresponding to an indentation of 100–200 nm, used in order to indent the cell wall only (Milani et al., 2011; Tvergaard and Needleman, 2018). The ramp size was of 2 μm (1000 data points per curve), approach speed of 100 μm/s and retract speed of 100 μm/s. For more details about cantilever calibration, see Bovio et al. (2019). Data analysis was done using JPK Data Processing software 6.0. Young's modulus was obtained by fitting the entire force versus tip-sample distance curve with a Hertz model for a sphere. For our analysis, we used a tip radius R of 400 nm and a Poisson's ratio v of 0.5 (as it is conventionally set for biological materials), where the Young's modulus, the point of contact, and an offset in force were kept as free parameters of the fit. In our analysis, only approach curves have been taken into account. Retract curves were obtained, but not used for further analysis. There are several reasons for this. First, in our case, adhesion forces are negligible compared with the setpoint force. Furthermore, although in the contact part of the approach curve the cantilever velocity is constant, this is not necessarily true for the contact part of retract curves. In fact, at the motion inversion point, that is at the beginning of the retract curve, the cantilever must be accelerated from 0 velocity up to the selected ramp speed. In the case of a viscoelastic material, as a plant tissue, this nonconstant speed may lead to variations in the apparent Young's modulus. For these reasons, we considered Young's modulus values extracted from approach curves as more reliable.

Laser Ablation

We carried out the laser ablation experiments on shoot apical meristems by using a Zeiss LSM 700 laser-scanning confocal microscope, equipped with an Andor MicroPoint (a galvanometer-based laser ablation system), which delivered a 6-Hz paused laser at 356 nm. Predissected meristems were cultured vertically in ACM for at least 4 h before the experiment. After being stained with propidium iodide (Sigma, 100 mM) for 5 minutes, the meristems were put under the microscope. Further steps were manipulated by using the iQ software from Andor. First, meristem was visualized to keep focus on the epidermis of meristem summit. Then we used the circular tool in iQ to draw a ROI with a diameter of 20 pixels (5 μm) at the center of the meristem. With a laser power at 8 with 5 repetitions for each point on the ROI, we made a circular wound. To assure the homogeneity of the ablations, the same procedure was carried on all wild-type and XyG mutant meristems.

Supplemental Data

The following supplemental materials are available.

Supplemental Figure S1. XyG distribution pattern in wild-type (Col) and XyG mutant shoot apices.

Supplemental Figure S2. Immunolocalization of XyGs in wild-type (Col) and XyG mutant shoot apex sections.

Supplemental Figure S3. Whole mount Immunolocalization of XyGs in wild-type (Col) and XyG mutant shoot apices.

Supplemental Figure S4. In situ hybridization of *XYL1*, *XXT1* and *XXT2* in wild-type shoot apices.

Supplemental Figure S5. Distribution of pectin and cellulose in *xyl1-4* and *xxt1xxt2* SAM.

Supplemental Figure S6. Distribution of other wall components in Col and *xxt1xxt2* SAM.

Supplemental Figure S7. Phenotype of xyloglucan mutants.

Supplemental Figure S8. No apparent torsion on *xyl1-4* and *xxt1xxt2* inflorescence stems.

Supplemental Figure S9. Microtubule patterning on SAMs of wild-type and XyG mutants.

ACKNOWLEDGMENTS

We thank Arezki Boudaoud for giving support on AFM measurement, Carlos S. Galvan-Ampudia for discussing the project, and Romain Azais for giving advice on statistical analyses.

Received June 13, 2019; accepted September 9, 2019; published September 19, 2019.

LITERATURE CITED

Armezzani A, Abad U, Ali O, Andres Robin A, Vachez L, Larrieu A, Mellerowicz EJ, Taconnat L, Battu V, Stanislas T, et al (2018) Transcriptional induction of cell wall remodelling genes is coupled to microtubule-driven growth isotropy at the shoot apex in *Arabidopsis*. Development **145:** dev162255

Barbier de Reuille P, Routier-Kierzkowska A-L, Kierzkowski D, Bassel GW, Schüpbach T, Tauriello G, Bajpai N, Strauss S, Weber A, Kiss A, et al (2015) MorphoGraphX: A platform for quantifying morphogenesis in 4D. eLife **4:** 5864

Baskin TI (2005) Anisotropic expansion of the plant cell wall. Annu Rev Cell Dev Biol **21:** 203–222

Besnard F, Refahi Y, Morin V, Marteaux B, Brunoud G, Chambrier P, Rozier F, Mirabet V, Legrand J, Lainé S, et al (2014) Cytokinin signalling inhibitory fields provide robustness to phyllotaxis. Nature **505:** 417–421

Blumenkrantz N, Asboe-Hansen G (1973) New method for quantitative determination of uronic acids. Anal Biochem **54:** 484–489

Boudaoud A, Burian A, Borowska-Wykręt D, Uyttewaal M, Wrzalik R, Kwiatkowska D, Hamant O (2014) FibrilTool, an ImageJ plug-in to quantify fibrillar structures in raw microscopy images. Nat Protoc **9:** 457–463

Boutté Y, Crosnier M-T, Carraro N, Traas J, Satiat-Jeunemaitre B (2006) The plasma membrane recycling pathway and cell polarity in plants: Studies on PIN proteins. J Cell Sci **119:** 1255–1265

Bovio S, Long Y, Monéger F (2019) Use of atomic force microscopy to measure mechanical properties and turgor pressure of plant cells and plant tissues. J Vis Exp **149:** e59674

Braybrook SA, Peaucelle A (2013) Mechano-chemical aspects of organ formation in *Arabidopsis thaliana*: The relationship between auxin and pectin. PLoS One **8:** e57813

Burk DH, Liu B, Zhong R, Morrison WH, Ye Z-H (2001) A katanin-like protein regulates normal cell wall biosynthesis and cell elongation. Plant Cell **13:** 807–827

Cavalier DM, Lerouxel O, Neumetzler L, Yamauchi K, Reinecke A, Freshour G, Zabotina OA, Hahn MG, Burgert I, Pauly M, et al (2008) Disrupting two *Arabidopsis thaliana* xylosyltransferase genes results in plants deficient in xyloglucan, a major primary cell wall component. Plant Cell **20:** 1519–1537

Cosgrove DJ (2018) Diffuse growth of plant cell walls. Plant Physiol **176:** 16–27

Cumming CM, Rizkallah HD, McKendrick KA, Abdel-Massih RM, Baydoun EA-H, Brett CT (2005) Biosynthesis and cell-wall deposition of a pectin-xyloglucan complex in pea. Planta **222:** 546–555

de Reuille PB, Bohn-Courseau I, Ljung K, Morin H, Carraro N, Godin C, Traas J (2006) Computer simulations reveal properties of the cell-cell signaling network at the shoot apex in Arabidopsis. Proc Natl Acad Sci USA **103:** 1627–1632

Faik A, Price NJ, Raikhel NV, Keegstra K (2002) An Arabidopsis gene encoding an α-xylosyltransferase involved in xyloglucan biosynthesis. Proc Natl Acad Sci USA **99:** 7797–7802

Feraru E, Feraru MI, Kleine-Vehn J, Martinière A, Mouille G, Vanneste S, Vernhettes S, Runions J, Friml J (2011) PIN polarity maintenance by the cell wall in Arabidopsis. Curr Biol **21:** 338–343

Galvan-Ampudia CS, Chaumeret AM, Godin C, Vernoux T (2016) Phyllotaxis: From patterns of organogenesis at the meristem to shoot architecture. Wiley Interdiscip Rev Dev Biol **5:** 460–473

Gruel J, Landrein B, Tarr P, Schuster C, Refahi Y, Sampathkumar A, Hamant O, Meyerowitz EM, Jönsson H (2016) An epidermis-driven mechanism positions and scales stem cell niches in plants. Sci Adv **2:** e1500989

Günl M, Pauly M (2011) AXY3 encodes a α-xylosidase that impacts the structure and accessibility of the hemicellulose xyloglucan in Arabidopsis plant cell walls. Planta **233:** 707–719

Hamant O, Heisler MG, Jönsson H, Krupinski P, Uyttewaal M, Bokov P, Corson F, Sahlin P, Boudaoud A, Meyerowitz EM, et al (2008) Developmental patterning by mechanical signals in Arabidopsis. Science **322:** 1650–1655

Heisler MG, Hamant O, Krupinski P, Uyttewaal M, Ohno C, Jönsson H, Traas J, Meyerowitz EM (2010) Alignment between PIN1 polarity and microtubule orientation in the shoot apical meristem reveals a tight coupling between morphogenesis and auxin transport. PLoS Biol **8:** e1000516

Kierzkowski D, Nakayama N, Routier-Kierzkowska A-L, Weber A, Bayer E, Schorderet M, Reinhardt D, Kuhlemeier C, Smith RS (2012) Elastic domains regulate growth and organogenesis in the plant shoot apical meristem. Science **335:** 1096–1099

Klavons JA, Bennett RD (1986) Determination of methanol using alcohol oxidase and its application to methyl ester content of pectins. J Agric Food Chem **34:** 597–599

Krupková E, Immerzeel P, Pauly M, Schmülling T (2007) The TUMOROUS SHOOT DEVELOPMENT2 gene of Arabidopsis encoding a putative methyltransferase is required for cell adhesion and co-ordinated plant development. Plant J **50:** 735–750

Kwiatkowska D, Dumais J (2003) Growth and morphogenesis at the vegetative shoot apex of Anagallis arvensis L. J Exp Bot **54:** 1585–1595

Kwiatkowska D, Routier-Kierzkowska A-L (2009) Morphogenesis at the inflorescence shoot apex of Anagallis arvensis: Surface geometry and growth in comparison with the vegetative shoot. J Exp Bot **60:** 3407–3418

La Rota C, Chopard J, Das P, Paindavoine S, Rozier F, Farcot E, Godin C, Traas J, Monéger F (2011) A data-driven integrative model of sepal primordium polarity in Arabidopsis. Plant Cell **23:** 4318–4333

Landrein B, Hamant O (2013) How mechanical stress controls microtubule behavior and morphogenesis in plants: History, experiments and revisited theories. Plant J **75:** 324–338

Landrein B, Refahi Y, Besnard F, Hervieux N, Mirabet V, Boudaoud A, Vernoux T, Hamant O (2015) Meristem size contributes to the robustness of phyllotaxis in Arabidopsis. J Exp Bot **66:** 1317–1324

Legland D, Arganda-Carreras I, Andrey P (2016) MorphoLibJ: Integrated library and plugins for mathematical morphology with ImageJ. Bioinformatics **32:** 3532–3534

Lerouxel O, Choo TS, Séveno M, Usadel B, Faye L, Lerouge P, Pauly M (2002) Rapid structural phenotyping of plant cell wall mutants by enzymatic oligosaccharide fingerprinting. Plant Physiol **130:** 1754–1763

Lin D, Cao L, Zhou Z, Zhu L, Ehrhardt D, Yang Z, Fu Y (2013) Rho GTPase signaling activates microtubule severing to promote microtubule ordering in Arabidopsis. Curr Biol **23:** 290–297

McFarlane HE, Döring A, Persson S (2014) The cell biology of cellulose synthesis. Annu Rev Plant Biol **65:** 69–94

Milani P, Gholamirad M, Traas J, Arnéodo A, Boudaoud A, Argoul F, Hamant O (2011) In vivo analysis of local wall stiffness at the shoot apical meristem in Arabidopsis using atomic force microscopy. Plant J **67:** 1116–1123

Milani P, Mirabet V, Cellier C, Rozier F, Hamant O, Das P, Boudaoud A (2014) Matching patterns of gene expression to mechanical stiffness at cell resolution through quantitative tandem epifluorescence and nanoindentation. Plant Physiol **165:** 1399–1408

Minic Z, Rihouey C, Do CT, Lerouge P, Jouanin L (2004) Purification and characterization of enzymes exhibiting β-D-xylosidase activities in stem tissues of Arabidopsis. Plant Physiol **135:** 867–878

Mouille G, Ralet MC, Cavelier C, Eland C, Effroy D, Hématy K, McCartney L, Truong HN, Gaudon V, Thibault JF, et al (2007) Homogalacturonan synthesis in Arabidopsis thaliana requires a Golgi-localized protein with a putative methyltransferase domain. Plant J **50:** 605–614

Neumetzler L, Humphrey T, Lumba S, Snyder S, Yeats TH, Usadel B, Vasilevski A, Patel J, Rose JK, Persson S, et al (2012) The FRIABLE1 gene product affects cell adhesion in Arabidopsis. PLoS One **7:** e42914

Park YB, Cosgrove DJ (2012) Changes in cell wall biomechanical properties in the xyloglucan-deficient xxt1/xxt2 mutant of Arabidopsis. Plant Physiol **158:** 465–475

Peaucelle A, Braybrook SA, Le Guillou L, Bron E, Kuhlemeier C, Höfte H (2011) Pectin-induced changes in cell wall mechanics underlie organ initiation in Arabidopsis. Curr Biol **21:** 1720–1726

Peaucelle A, Louvet R, Johansen JN, Höfte H, Laufs P, Pelloux J, Mouille G (2008) Arabidopsis phyllotaxis is controlled by the methyl-esterification status of cell-wall pectins. Curr Biol **18:** 1943–1948

Pedersen HL, Fangel JU, McCleary B, Ruzanski C, Rydahl MG, Ralet M-C, Farkas V, von Schantz L, Marcus SE, Andersen MCF, et al (2012) Versatile high resolution oligosaccharide microarrays for plant glycobiology and cell wall research. J Biol Chem **287:** 39429–39438

Pfeiffer A, Wenzl C, Lohmann JU (2017) Beyond flexibility: Controlling stem cells in an ever changing environment. Curr Opin Plant Biol **35:** 117–123

Reinhardt D, Pesce E-R, Stieger P, Mandel T, Baltensperger K, Bennett M, Traas J, Friml J, Kuhlemeier C (2003) Regulation of phyllotaxis by polar auxin transport. Nature **426:** 255–260

Rizk SE, Abdel-Massih RM, Baydoun EA-H, Brett CT (2000) Protein- and pH-dependent binding of nascent pectin and glucuronoarabinoxylan to xyloglucan in pea. Planta **211:** 423–429

Rozier F, Mirabet V, Vernoux T, Das P (2014) Analysis of 3D gene expression patterns in plants using whole-mount RNA in situ hybridization. Nat Protoc **9:** 2464–2475

Sampedro J, Pardo B, Gianzo C, Guitián E, Revilla G, Zarra I (2010) Lack of α-xylosidase activity in Arabidopsis alters xyloglucan composition and results in growth defects. Plant Physiol **154:** 1105–1115

Sampedro J, Sieiro C, Revilla G, González-Villa T, Zarra I (2001) Cloning and expression pattern of a gene encoding an α-xylosidase active against xyloglucan oligosaccharides from Arabidopsis. Plant Physiol **126:** 910–920

Sassi M, Ali O, Boudon F, Cloarec G, Abad U, Cellier C, Chen X, Gilles B, Milani P, Friml J, et al (2014) An auxin-mediated shift toward growth isotropy promotes organ formation at the shoot meristem in Arabidopsis. Curr Biol **24:** 2335–2342

Sechet J, Frey A, Effroy-Cuzzi D, Berger A, Perreau F, Cueff G, Charif D, Rajjou L, Mouille G, North HM, et al (2016) Xyloglucan metabolism differentially impacts the cell wall characteristics of the endosperm and embryo during Arabidopsis seed germination. Plant Physiol **170:** 1367–1380

Sechet J, Htwe S, Urbanowicz B, Agyeman A, Feng W, Ishikawa T, Colomes M, Kumar KS, Kawai-Yamada M, Dinneny JR, et al (2018) Suppression of Arabidopsis GGLT1 affects growth by reducing the L-galactose content and borate cross-linking of rhamnogalacturonan-II. Plant J **96:** 1036–1050

Smyth DR, Bowman JL, Meyerowitz EM (1990) Early flower development in Arabidopsis. Plant Cell **2:** 755–767

Stanislas T, Platre MP, Liu M, Rambaud-Lavigne LES, Jaillais Y, Hamant O (2018) A phosphoinositide map at the shoot apical meristem in *Arabidopsis thaliana*. BMC Biol **16:** 20

Tvergaard V, Needleman A (2018) Effect of properties and turgor pressure on the indentation response of plant cells. J Appl Mech **85:** 61007

Uyttewaal M, Burian A, Alim K, Landrein B, Borowska-Wykręt D, Dedieu A, Peaucelle A, Ludynia M, Traas J, Boudaoud A, et al (2012) Mechanical stress acts via katanin to amplify differences in growth rate between adjacent cells in Arabidopsis. Cell **149:** 439–451

Verger S, Long Y, Boudaoud A, Hamant O (2018) A tension-adhesion feedback loop in plant epidermis. eLife **7:** e34460

Xiao C, Zhang T, Zheng Y, Cosgrove DJ, Anderson CT (2016) Xyloglucan deficiency disrupts microtubule stability and cellulose biosynthesis in Arabidopsis, altering cell growth and morphogenesis. Plant Physiol **170:** 234–249

Yang W, Schuster C, Beahan CT, Charoensawan V, Peaucelle A, Bacic A, Doblin MS, Wightman R, Meyerowitz EM (2016) Regulation of meristem morphogenesis by cell wall synthases in Arabidopsis. Curr Biol **26:** 1404–1415

Zabotina OA, Avci U, Cavalier D, Pattathil S, Chou Y-H, Eberhard S, Danhof L, Keegstra K, Hahn MG (2012) Mutations in multiple XXT genes of Arabidopsis reveal the complexity of xyloglucan biosynthesis. Plant Physiol **159:** 1367–1384

Zhao F, Zheng Y-F, Zeng T, Sun R, Yang J-Y, Li Y, Ren D-T, Ma H, Xu Z-H, Bai S-N (2017) Phosphorylation of SPOROCYTELESS/NOZZLE by the MPK3/6 kinase is required for anther development. Plant Physiol **173:** 2265–2277